Research Article

Enhancement of photoresponsive electrical characteristics of multilayer MoS$_2$ transistors using rubrene patches

Eun Hei Cho[1], Won Geun Song[2], Cheol Joon Park[1], Jeongyong Kim[3], Sunkook Kim[2] (✉), and Jinsoo Joo[1] (✉)

[1] *Department of Physics, Korea University, Seoul 136-713, R. O. Korea*

[2] *Department of Electronics and Radio Engineering Institute for Laser Engineering, Kyung Hee University, Yongin, Gyeonggi-do 446-701, R. O. Korea*

[3] *Center for Integrated Nanostructure Physics (CINAP), Institute for Basic Science (IBS); Department of Energy Science, Sungkyunkwan University, Suwon 440-746, R. O. Korea*

ABSTRACT

Multilayer MoS$_2$ is a promising active material for sensing, energy harvesting, and optoelectronic devices owing to its intriguing tunable electronic band structure. However, its optoelectronic applications have been limited due to its indirect band gap nature. In this study, we fabricated a new type of phototransistor using multilayer MoS$_2$ crystal hybridized with p-type organic semiconducting rubrene patches. Owing to the outstanding photophysical properties of rubrene, the device characteristics such as charge mobility and photoresponsivity were considerably enhanced to an extent depending on the thickness of the rubrene patches. The enhanced photoresponsive conductance was analyzed in terms of the charge transfer doping effect, validated by the results of the nanoscale laser confocal microscope photoluminescence (PL) and time-resolved PL measurements.

1 Introduction

Two-dimensional (2D) nanosheets (NSs) such as graphene and their multilayered structures have received considerable attention owing to their interesting intrinsic properties and wide range of applications for future electronic devices [1, 2]. Graphene has a conical Dirac spectrum of energy states without a band gap, resulting in fascinating electrical properties [1–3]. However, the gapless band structure of graphene makes it unsuitable as an electronic switching material in conventional transistors and photoresponsive devices.

Recently, new 2D hexagonal-shaped semiconducting NSs such as transition metal dichalcogenides have been intensively studied as promising low-dimensional active materials for optoelectronic devices

[4–6]. The graphene-like hexagonal form of MX_2 (where M = metal and X = S, Se, or Te) are layered with covalent bonds between the X–M–X atoms, and the layers are weakly held together by van der Waals interactions [7]. In particular, MoS_2 has been investigated for applications to chemical vapor sensing [8, 9], energy harvesting [10], and optoelectronic devices [11] because of its intriguing tunable electronic band structure resulting from the atomically controlled thickness of the layer [12]. In MoS_2 bulk structures, because of broken symmetry, the bulk MoS_2 shows an indirect band gap of ~1.3 eV, whereas the monolayer MoS_2 has a direct band gap of ~1.8 eV.

Thin-film transistors (TFTs) that use monolayer MoS_2 showed good device performance such as a high I_{ON}/I_{OFF} ratio of ~10^8, low subthreshold swing (SS) of ~70 mV/decade [4, 13], and mobility range from ~1 to ~200 cm^2/V·s depending on the dielectric constants of the capping environment (air or HfO_2). The multilayer MoS_2-based TFTs also exhibited stable device performance such as near-ideal SS of ~70 mV/decade, high mobility of ~100 cm^2/V·s, and robust current saturation over a large voltage window [14]. However, in spite of the merits of the multilayer MoS_2 TFTs with three times the density of states of the monolayer form, structural defects [13] and charge traps [15] from the environment could induce device degradation. Furthermore, photodetectors using multilayer MoS_2 have shown a poor photoresponsivity of ~100 mA/W because of their indirect band gap nature [16], whereas the photoresponsivity of those that use the monolayer MoS_2 was measured as ~880 A/W [17].

The enhanced charge carrier mobility of the monolayer MoS_2 TFTs that use HfO_2 or polymer electrolyte capping layers [4, 18] was attributed to the suppression of the Coulomb scattering due to the high-κ dielectric environment and the modification of phonon dispersion in the MoS_2 material. As promising photosensitive capping materials, organic π-conjugated small molecules such as rubrene are recommended for MoS_2-based hybrid optoelectronic devices because of their superior photophysical p-type semiconducting characteristics under light emission [19]. The intrinsic and device characteristics of multilayered MoS_2 hybrids with organic semiconducting patches have not been thoroughly studied yet.

In the present study, we investigate the optoelectronic properties of MoS_2 TFTs hybridized with p-type organic rubrene patches. Enhancement in the device performance, such as carrier mobility and photoresponsivity, was achieved by the hybridization of rubrene patches in the MoS_2 channel. The photophysical dynamics of the MoS_2/rubrene-patch hybrids were studied using laser confocal photoluminescence (PL) spectra and time-resolved (TR)-PL spectra. Depending on the thickness of the rubrene patches, we observed a considerable increase in the photocurrent and carrier mobility of the hybrid MoS_2/rubrene-patch TFTs, which were analyzed in terms of the charge transfer (CT) doping effect between the p-type organic rubrene patches and n-type MoS_2 crystal.

2 Experimental

2.1 Fabrication of MoS₂ transistors

Multilayer MoS_2 flakes were mechanically exfoliated from bulk MoS_2 crystals and transferred to a SiO_2/Si substrate. A highly doped p-type Si wafer (resistivity < 5 × 10^{-3} Ω·cm) coated with 300 nm SiO_2 was used for the gate of the MoS_2 transistors. Electrical contacts (100 μm × 100 μm) were patterned at the top of the MoS_2 flakes using a conventional lift-off technique. Ti (10 nm) and Au (300 nm) were deposited by electron-beam evaporation at room temperature. The device was then annealed at 200 °C in a vacuum tube furnace for 2 h (100 sccm Ar and 10 sccm H_2) to remove the resist residue and to decrease the contact resistance.

2.2 Deposition of rubrene

Rubrene molecules were deposited on the surface of the MoS_2 layer using an organic thermal evaporation system (Dae Ki Hi-Tech Co. Ltd.) [20]. Rubrene molecules were grown in ultra-high vacuum (1.7 × 10^{-7} Torr) at 130 °C. The growth rate (1 Å/min) was finely controlled to obtain rubrene patches with a nanometer-scale thickness. The rubrene deposition was repeated three times to obtain thicker patches.

2.3 Measurements

To measure the thicknesses of the MoS_2 crystal and

rubrene patches, an atomic force microscope (AFM) (Nano-Focus Ltd., Albatross)-equipped laser confocal microscope (LCM) system was used. For the LCM PL experiments, a He–Ar laser (λ_{ex} = 488 nm) was used for the PL excitation. The spot size of the focused laser beam on the sample in the LCM system was estimated to be approximately 200 nm. The incident laser power on the sample and the acquisition time for each PL spectrum were 10 µW and 20 ms, respectively. The detailed methods of the LCM experiment have been previously reported [21]. The photoresponsive electrical characteristics of the devices were measured in vacuum (CTI-Cryogenic cryostat) using a source-measurement unit (SMU) guaranteed for the measurement resolution and accuracy as 10 pA and ±(0.04% + 60 pA), respectively, (Keithley 237, USA). Two types of collimated LED lamps (Thorlabs, λ = 455 and 633 nm) were used for light irradiation of the TFTs.

3 Results and discussion

3.1 Preparation of hybrid MoS$_2$/rubrene-patch TFTs and energy band structure

A 300-nm-thick cleaned-surface SiO$_2$/p++ Si wafer was chosen for the substrate of our n-type multilayer MoS$_2$ TFTs with top-contact Au/Ti (300 nm/20 nm) electrodes. Figure 1(a) shows a schematic illustration of the hybrid MoS$_2$/rubrene-patch TFT. The thickness of the 2D MoS$_2$ crystal was approximately 60 nm, and the channel length of the TFT was ~10 µm with a width/length (*W/L*) ratio of ~6, as shown in Figs. 1(a) and 1(b). The deposition of the rubrene on the surface of the MoS$_2$ layer was performed three times in a row using an organic thermal evaporation system [20]. Rubrene patches, represented by the small bright spots in the insets of Figs. 1(b) and 1(c) (AFM images) were formed on the MoS$_2$ surface, and their thickness (t_R) and size were gradually increased (Fig. 1(c)) by
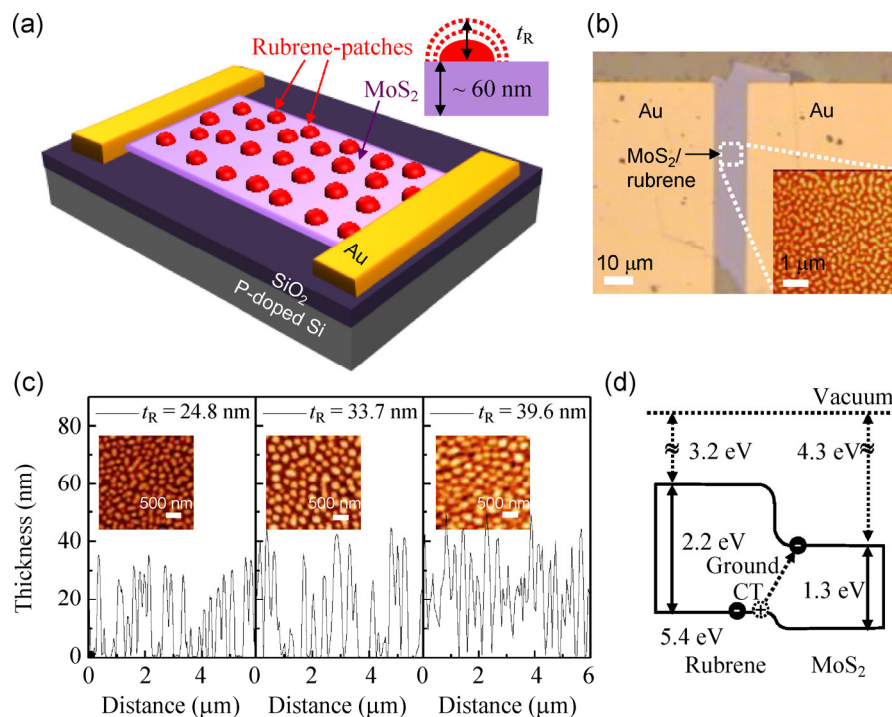

Figure 1 (a) Schematic illustration of the hybrid MoS$_2$/rubrene-patch TFT. Inset: Schematic illustration of the thickness variation of rubrene patches on the MoS$_2$ channel. (b) Optical microscope image of the hybrid MoS$_2$/rubrene-patch TFT. Inset: AFM image of the hybrid MoS$_2$/rubrene-patch channel. The small brighter spots represent the rubrene patches. (c) Cross-sectional plots and their AFM images (insets) of the rubrene patches on the MoS$_2$ channel with (left) t_R = 24.8 ± 7.9 nm, (middle) 33.7 ± 7.6 nm, and (right) 39.6 ± 6.0 nm. (d) Schematic energy band diagram of the p–n heterojunction of the MoS$_2$/rubrene patches for the explanation of the ground CT effect.

increasing the deposition times. Figure 1(c) shows the cross-sectional surface profiles and the corresponding AFM images of the rubrene patches on the MoS$_2$ surface with the same nanometer scale. The t_R values of the rubrene patches were measured to be 24.8 ± 7.9 nm, 33.7 ± 7.6 nm, and 39.6 ± 6.0 nm for the first, second, and third rubrene deposition, respectively. It is noted that these thicknesses are in the range of the exciton diffusion length for organic semiconducting materials (few tens of nanometers) [22, 23]. By increasing the physical size of the rubrene patches, the density value of the patches decreased from approximately 19 to 12 μm^{-2} for the first and third deposition, respectively. However, the rubrene patches still exhibited discontinuous distribution in all cases.

Figure 1(d) shows the schematic energy band diagram of the p–n heterojunction of the rubrene and MoS$_2$. The energy band gaps of the rubrene and MoS$_2$ in this study were 2.2 and 1.3 eV [24], respectively. The conduction band edge of MoS$_2$ is higher than the level of the high occupied molecular orbital (HOMO) of rubrene (5.4 eV) by approximately 1.1 eV, as shown in Fig. 1(d). It is noted that the Fermi energy level (E_F) in the bulk MoS$_2$ crystal is formed at 4 meV near the conduction band edge at room temperature when the carrier density is about $n = 5 \times 10^{13}$/cm^2 [14]. Because of the variation in the hole and electron concentration across the unbiased p–n heterojunction, an interfacial ground CT across the HOMO energy level of rubrene to the conduction band edge of MoS$_2$ can occur, resulting in the Coulombically bound electron and hole pair at the MoS$_2$/rubrene-patch interface that possesses a dipole momentum (CT exciton). The additional charges due to the ground CT effect could fill the trap sites in the MoS$_2$ layer and the interface. By applying the bias, the CT excitons are successfully dissociated and transported to the counter electrodes. Therefore, the current enhancement of the hybrid devices due to the ground CT doping effect can be observable under dark conditions.

3.2 Photophysical characteristics of hybrid MoS$_2$ and rubrene patches: CT effect

The rubrene-patched MoS$_2$ crystals were prepared on the SiO$_2$/Si substrate to study the CT doping effect, as shown in Fig. 2. For the measurement of the

nanoscale PL image and spectra, a high-resolution (≤200 nm) LCM equipped with a He–Ar laser (λ_{ex} = 514 nm, laser power = 10 μW; sufficiently selective to excite only the rubrene patches) was used. Figure 2(a) shows the optical microscope image (top) and LCM PL image (bottom) of the hybrid MoS$_2$/rubrene patches. Exfoliated multilayer MoS$_2$ crystals with a thickness of 20–30 nm were placed on the SiO$_2$/Si substrate, and rubrene patches with a thickness of 25–40 nm were then deposited on the surface of the MoS$_2$ crystal. We observed the formation of discontinuous islands of rubrene patches (small brighter spots in Fig. 2(a)). Regions A and B in the top image
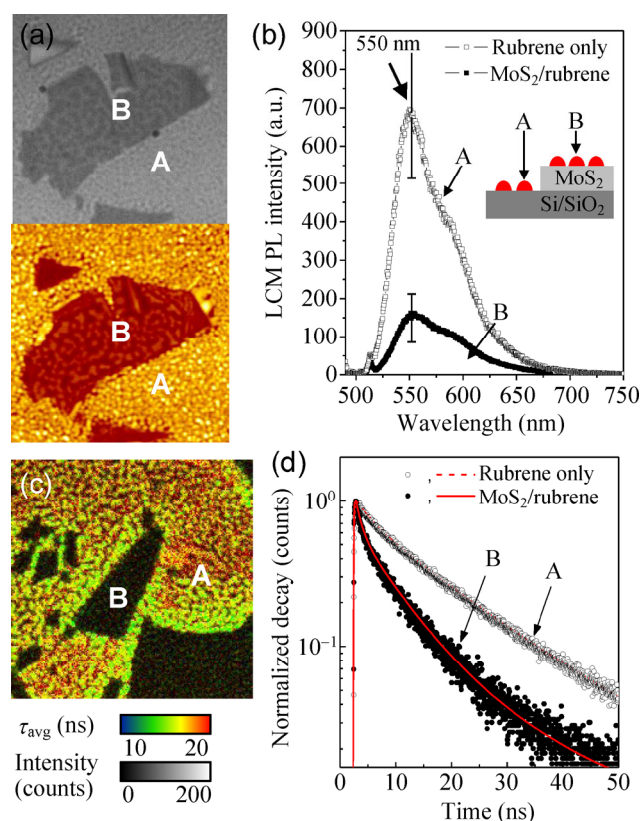

Figure 2 (a) (Top) optical microscope image and (bottom) confocal PL image of the rubrene patches on the MoS$_2$ crystal/SiO$_2$/Si substrate. The rubrene patches are located on different substrates (Region A: SiO$_2$/Si substrate; region B: MoS$_2$ crystal/SiO$_2$/Si substrate). (b) LCM PL spectra of the rubrene patches in corresponding regions A and B. Inset: Schematic illustration of the discontinuous rubrene patches on the SiO$_2$/Si substrate and the MoS$_2$ crystal/SiO$_2$/Si substrate. (c) TR-PL mapping image of the pristine MoS$_2$ and hybrid MoS$_2$/rubrene patches (relatively darker regions). (d) TR-PL decay curves of the rubrene patches on different substrates (Region A: SiO$_2$/Si substrate; region B: MoS$_2$ crystal/SiO$_2$/Si substrate).

of Fig. 2(a) correspond to the rubrene patches on the SiO$_2$/Si substrate (i.e., without MoS$_2$) and on the MoS$_2$ crystal, respectively. At the surface of the MoS$_2$ crystal (region B), the brightness of the rubrene luminescence was selectively reduced (i.e., quenched) compared with that of the pristine rubrene PL in region A, as shown in Fig. 2(a).

Figure 2(b) shows the nanoscale LCM PL characteristics of a single rubrene patch. The LCM PL spectra of the pristine rubrene patches (in region A) and the rubrene patches on the MoS$_2$ crystal (in region B) were measured for 10 different spots, and the average was obtained. The yellow–green PL peak of the pristine rubrene patches was observed at ~550 nm, associated with singlet excitons. The average LCM PL intensity considerably decreased by approximately 75% for the hybrid MoS$_2$/rubrene-patch structure (region B), as shown in Fig. 2(b). The thicknesses of the rubrene patches (25–40 nm) were comparable with the exciton diffusion length in organic materials (few tens of nanometers). It is suggested that the exciton generated in the rubrene patches could migrate to the interface between the rubrene and MoS$_2$, resulting in the CT interaction at the heterojunctions. The fast diffusion of the singlet excitons in the rubrene patches induced the distinct fluorescence quenching of rubrene PL mostly via a non-radiative process.

To study the fluorescence quenching and CT effect in the time scale, the time-resolved-photoluminescence (TR-PL) mapping images and spectra of the exciton lifetime of the MoS$_2$/rubrene-patch hybrid structure were measured, as shown in Figs. 2(c) and 2(d), respectively. For the selective collection of photons using the corresponding energy of a singlet exciton, a TR fluorescence confocal microscope (Micro Time-200, PicoQuant GN003) with a diode laser (λ_{ex} = 375 nm) and a band-pass filter (centered at 550 nm, full width at half maximum (FWHM) = 40 nm) were used. The resulting emissions were collected by time-correlated single-photon counting with a time resolution and an FWHM instrument response function of 4 and 240 ps, respectively. In Fig. 2(c), the imaging resolution of the confocal mapping was approximately 180 nm, and both exciton lifetime (τ_{avg}) and PL intensity (photon counts) information are shown by the scale bars (at the bottom). Regions A and B represent the same corresponding

area as that in Fig. 2(a). In hybrid region B of the MoS$_2$/rubrene patches, the fluorescence lifetime decreased markedly in comparison with that of the pristine rubrene patches (region A), as shown in Fig. 2(c). The fluorescence decay curves were analyzed in terms of the multi-exponential model given by $I(t) = \Sigma A_i \exp(-t/\tau_i)$, where A_i and τ_i are the amplitude and the fluorescence lifetime of the ith component, respectively. The amplitude-weighted average lifetimes (τ_{avg}) were calculated by $\tau_{avg} = \Sigma(A_i \tau_i)/\Sigma(A_i)$ [25]. In general, rubrene crystals have two characteristic decay processes, namely, the fast and the long PL with average lifetimes of ~15 ns and ~1 μs, respectively [26]. The yellow–green PL originated from the short-lived singlet excitons. In contrast, the red PL was observed on the long timescale of over 1 μs, consistent with the triplet–triplet fusion process linked to phosphorescence in organic materials [27]. For our samples, the τ_{avg} values of the yellow–green PL of the rubrene patches were estimated to be approximately 12.6 and 5.2 ns (decreased by 59%) in regions A and B, respectively (also listed in Table 1). The distinct reduction in the fluorescence intensity (quenching) and fluorescence lifetime of the rubrene patches on the surface of the multilayer MoS$_2$ crystal originated because the photoexcited Frenkel singlet excitons of rubrene were sufficiently dissociated to the CT states at the p–n heterojunction between the MoS$_2$ and rubrene. Therefore, we consider that the hybrid structure of the rubrene-patched MoS$_2$ crystal can be applied as a new active layer in 2D optoelectronic applications.

3.3 Comparative *I–V* characteristics of the pristine and hybrid MoS$_2$/rubrene-patch TFTs under dark conditions

Figure 3(a) shows the output source–drain current characteristic curves (I_D–V_D) of the pristine MoS$_2$

Table 1 Multi-components (A_i, τ_i) and τ_{avg} for fitting of the fluorescence decay lifetime curves of the pristine rubrene and MoS$_2$/rubrene-patch samples

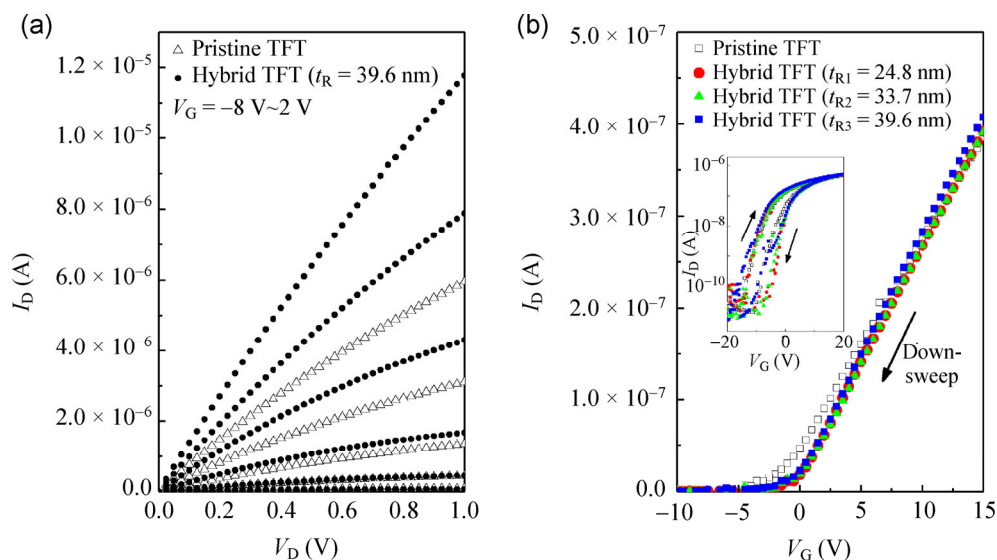| Sample	Multi-components				τ_{avg} (ns)
Rubrene	A_i	821.5	2194.4	597.7	12.6
	τ_i (ns)	2.8	13.1	24.1	
Rubrene on MoS$_2$	A_i	333.0	350.7	76.5	5.2
	τ_i (ns)	1.0	6.6	17.6	

Figure 3 (a) Output characteristic curves (I_D versus V_D) of the pristine MoS_2 and hybrid MoS_2/rubrene-patch (t_{R3} = 39.6 nm) TFTs under dark conditions. (b) Transfer characteristic curves (I_D versus V_G) of the pristine and hybrid MoS_2/rubrene-patch TFTs under dark conditions. The arrows represent the directions of the gate bias sweep. Inset: Hysteresis transfer characteristic curves (I_D versus V_G) in a logarithmic scale of the corresponding TFTs during the down- and up-sweeps.

(open markers) and hybrid MoS_2/rubrene-patch (solid markers) TFTs under dark conditions. The I_D–V_D characteristic curves were measured with various gate biases (V_G) of –10, –8, –6, –4, –2, 0, and 2 V. The output I_D–V_D curves of the pristine MoS_2 TFTs exhibited n-type linear characteristics attributed to the absence of channel pinch-off. Increasing V_G lowered the barriers at the electrode contacts; thus, I_D increased linearly. After the deposition of rubrene patches (t_R = 39.6 nm) on the MoS_2 channel, I_D markedly increased, and the non-saturation behavior in the output I_D–V_D characteristic curves became severe over the whole measurement range, as shown in Fig. 3(a). These results indicate that the electrical conduction of the MoS_2 TFTs under dark conditions increased after the deposition of rubrene patches because of the accumulated additional charges due to the formation of the p–n junction between the MoS_2 and rubrene patches. These additional charge carriers of the dark current were attributed to the interfacial ground state CT that occurred from the HOMO energy level of rubrene to the conduction band edge of the MoS_2 crystal (Fig. 1(d)). This process induced extra free electrons at the conduction band edge of MoS_2, and thus the activation energy in the MoS_2 channel could be reduced [28]. In previous reports for molybdenum dithiolene complexes with a p-type organic material

dopant, the formation of a narrow depletion region in the channel material by charge doping induced a variation in the charge transport properties [29, 30]. The charge doping effect on the monolayer MoS_2 using Au nanoparticles was also reported [31]. Similar I_D–V_D characteristics were observed for the other hybrid MoS_2/rubrene-patches TFTs with different thickness of the rubrene (see Figs. S1 and S2 in the Electronic Supplementary Material (ESM)).

Figure 3(b) shows the gate bias-dependent I_D characteristic curves (at V_D = 10 mV) of the pristine and hybrid MoS_2 TFTs with three different thicknesses (t_{R1} = 24.8 nm, t_{R2} = 33.7 nm, and t_{R3} = 39.6 nm) of rubrene patches under dark conditions. The linear mobility (μ_{lin}) was obtained from the following equation: μ_{lin} = $(dI_D/dV_G)/(C_{ox}V_D) \cdot (L/W)$, where dI_D/dV_G and C_{ox} represent the transconductance and gate-dielectric capacitance, respectively. Interestingly, the μ_{lin} values obtained from the down-sweep curves gradually increased from μ_{pri} = 34.3 cm²/V·s for the pristine MoS_2 TFT to μ_{R1} = 38.1 cm²/V·s, μ_{R2} = 39.8 cm²/V·s, and μ_{R3} = 42.3 cm²/V·s for the hybrid MoS_2/rubrene-patch TFTs with increasing rubrene-patch thickness. In the previous reports, the μ_{lin} value of the multilayered MoS_2 TFTs on the SiO_2 dielectric material was ~10 cm²/V·s [16, 32]. The enhanced charge carrier mobility of the hybrid MoS_2/rubrene-patch TFTs in

the present study indicates the active CT doping effect and the fast diffusion of the doped charges. Supporting evidence for the CT doping effect is also provided by the results of the LCM PL and the TR-PL measurements (Fig. 2). In other previous reports, the interfacial CT doping induced filling of the surface charge traps and contributed to the accumulation of mobile charge carriers at the channels [29, 30]. In addition, the poor device performance such as phonon-limited low mobility could be improved through Schottky barrier lowering caused by the CT doping in the thin dielectric layer even in the presence of non-ideal channel/dielectric interfaces [33]. The conductance of the active layer between source and drain is proportional to both charge density (n) and mobility (μ). Therefore, the CT doping effect by the rubrene patches contributed to increase the charge density and mobility, resulting in the considerable enhancement of I_D level (i.e., conductance) in Fig. 3(a).

The nanostructures of rubrene patches in this study were designed for the efficient CT doping in the hybrid MoS$_2$/rubrene TFTs. If the rubrene patches are formed as the top sheet (i.e., a different whole layer) over MoS$_2$, p-type and n-type electrical channels due to the rubrene sheet and MoS$_2$ crystal, respectively, could be generated, resulting in the different device performance of TFTs. Discontinuous rubrene patches—such as nanoislands—can be effective doping system for the MoS$_2$ layer to improve the transistor characteristics. A previous study also showed how transistor performance could be optimized using organic nano-patches [28].

The inset of Fig. 3(b) shows the gate bias-dependent I_D characteristic curves of the same TFTs shown in Fig. 3(a) during both down-sweeping and up-sweeping in which the hysteresis transfer characteristics of both the pristine and hybrid TFTs are observed. After the deposition of rubrene patches, the transfer curve (up-sweeping) was shifted to the left side and the threshold voltage (V_T) was changed from –6.8 V to –8.2 V (i.e., lowering V_T) for the pristine MoS$_2$ and hybrid MoS$_2$/rubrene-patch (t_R = 39.6 nm) TFTs, relatively (Fig. S3 in the ESM). The n-doping effect can be attributed to the rubrene patches. The hysteresis I–V curves of the TFTs originated from the charge trapping and de-trapping effects at the localized defects sites and interfaces [34]. The width of the hysteresis of the hybrid MoS$_2$/rubrene-patch TFTs was larger than that of the pristine MoS$_2$ TFT. In our devices, a uniform electric field over the MoS$_2$ crystal can be expected; therefore, the main reason for the increasing hysteresis width could be the activation of the charge trapping and de-trapping behavior of the CT doping from the adsorbed rubrene patches. From these results, the enhancement of the transistor characteristics (e.g., enhanced I_D and μ_{lin}) and the CT doping effects through the hybridization of the p-type rubrene patches in the MoS$_2$ TFTs were successfully demonstrated.

3.4 Photoresponsive *I–V* characteristics of the hybrid MoS$_2$/rubrene-patch TFTs

Figure 4(a) shows the transfer characteristic curves (I_D versus V_G) of the pristine MoS$_2$ and hybrid MoS$_2$/rubrene-patch (t_{R3} = 39.6 nm) TFTs at V_D = 10 mV in the dark and under light irradiation. Two different light sources, namely, λ = 455 and 633 nm (P_{in} = 4 mW/cm^2), were used to investigate the photo-responsive I_D–V_G characteristics of the devices. To explain the charge transport mechanism of the TFTs, Figs. 4(b) and 4(c) show the schematic energy band diagrams of the photoresponsive electrical conduction of the MoS$_2$/rubrene-patch TFTs in the OFF (I_{OFF}) and ON (I_{ON}) states, respectively. In the OFF state (V_G < V_T), the I_D levels were more sensitive to both the applied negative V_G and incident light, as shown in Fig. 4(a). The illumination induced the formation of excitons in rubrene, and the dissociated electrons and holes in the MoS$_2$ channel due to the application of V_D contributed to the total I_D through the photoinduced CT. In OFF state, when the photoinduced charges were accumulated in the MoS$_2$ channel, the two Au electrodes were electrically connected and then, the effective OFF state photocurrent could be generated. It is noted that the I_D values in the OFF state in Fig. 4(a) were higher than the minimum current level of the SMU system. Therefore, both ground and photoinduced CT effects enhanced I_D in the hybrid MoS$_2$/rubrene-patch TFTs, as shown in Fig. 4(b). In the ON state (Fig. 4(c), V_G > V_T), the I_D levels were less sensitive to the incident light, and the thermionic and tunneling currents dominated the electrical conduction in the MoS$_2$ channel.
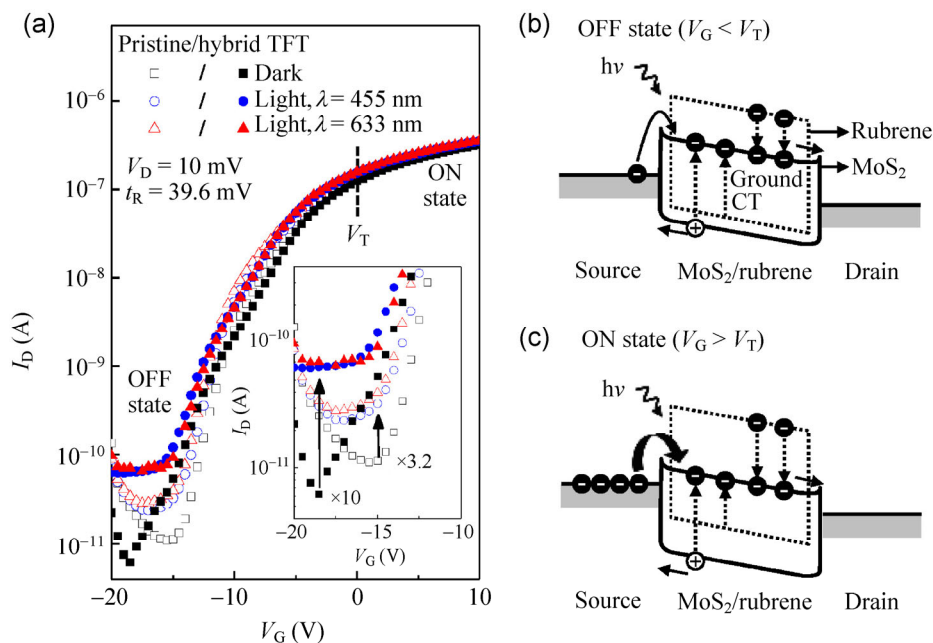
Figure 4 (a) Transfer characteristic curves (I_D versus V_G) in logarithmic scale of the pristine MoS_2 and hybrid MoS_2/rubrene-patch TFTs (t_{R3} = 39.6 nm) in the dark and under light irradiation (λ = 455 and 633 nm). The dashed line represents the boundary (V_T) of the OFF and ON states. Inset: Magnified transfer characteristic curves in the OFF regime ($V_G \leqslant$ −10 V). Schematic energy band diagrams of the hybrid MoS_2/rubrene-patch TFTs under illumination in (b) OFF and (c) ON states. The dashed boxes represent the energy band diagram of rubrene.

At high positive V_G values ($V_G \geqslant$ 5 V), the I_{ON} levels of all the TFTs were very weakly changed after the rubrene hybridization under light irradiation, as shown in Fig. 4(a). However, with a negative gate bias ($V_G \leqslant$ −10 V), we observed a considerable variation in the transfer characteristic curves of both the pristine and hybrid TFTs with light irradiation. With high negative V_G values, the I_{OFF} values (open markers) of the pristine MoS_2 TFTs increased under light irradiation (λ = 455 and 633 nm). For example, the ratio of the I_{OFF} values between the photoinduced and the dark currents (I_{light}/I_{dark}) was ~3.2 (λ = 455 nm at V_G = −15 V), as shown in the inset in Fig. 4(a). After the deposition of the rubrene patches, the I_{light}/I_{dark} ratio markedly increased to a value of ~10 at V_G = −18.5 V. These results imply that the photoinduced singlet excitons from the rubrene patches were distinctly quenched via a non-radiative process, and they contributed to the increase in the photocurrent through the dissociated electrons and holes in the hybrid MoS_2/rubrene-patch TFTs (please see Fig. 4(b)). For the pristine MoS_2 TFTs, the photoresponsive I_D (red open-triangle markers) in the OFF state under red light irradiation (λ = 633 nm) showed more sensitive variation compared with that

under blue light irradiation (λ = 455 nm) (blue open-circle makers in the inset of Fig. 4(a)) because the 633 nm incident light well matched with the absorption band of the MoS_2. However, the photoresponsive I_{OFF} values of the hybrid MoS_2/rubrene-patch TFTs had similar current levels under the red or blue light irradiation because the 455 nm incident light well matched with the absorption band of the rubrene material, whereas the pristine MoS_2 TFTs showed more active photoresponsive characteristics under the red light irradiation (λ = 633 nm). In summary, the photoresponsive I_D values of the MoS_2 TFTs considerably increased at high negative gate biases after the deposition of the rubrene patches and selectively responded to the specific light irradiation (well matched with their light absorption spectrum). However, I_{ON} (i.e., high positive bias) in the charge accumulation regime of the hybrid MoS_2/rubrene-patch TFTs showed relatively weak photoresponsive electrical characteristics. These photoresponsive electrical characteristics of the pristine and hybrid MoS_2/rubrene-patch TFTs were reproduced for other TFT devices (see Fig. S1 in the ESM). It was confirmed that the hybridization of rubrene patches on

the MoS$_2$ channel induced the enhancement of the photoresponsive electrical properties of the multilayer MoS$_2$ TFTs.

3.5 Photoresponsivity of the hybrid TFTs with different rubrene-patch thicknesses

Figure 5(a) shows the transfer characteristic curves (I_D versus V_G) at V_D = 10 mV of the pristine and hybrid MoS$_2$ TFTs with three different rubrene-patch thicknesses in the dark and under light irradiation (λ = 455 nm, P_{in} = 15 mW/cm^2). The rubrene-patch thicknesses of the hybrid TFTs were 28.8 nm (t_{R1}), 33.7 nm (t_{R2}), and 39.6 nm (t_{R3}). With the increase in the rubrene-patch thickness, the photoresponsive I_D gradually increased in the I_{OFF} state regime ($V_G \leqslant$ –10 V), as shown in Fig. 5(a) and its inset. At V_G = –15.5 V, the photoresponsive I_D values of the hybrid MoS$_2$/rubrene-patch TFTs gradually increased to ~2, ~2.6, and ~3.8 with the increase in the rubrene-patch thickness from 24.8, 33.7, and 39.6 nm, respectively, compared with the reference values of the pristine MoS$_2$ TFTs. These results suggest that for the hybrid MoS$_2$/rubrene-patch TFTs, more photoinduced charge carriers, including the ground state CT carriers due to the

hybridization of the p-type rubrene patches, contributed to the electrical conduction in the MoS$_2$ channel.

Figure 5(b) shows the gate bias-dependent photoresponsivity (R) characteristic curves at V_D = 10 mV of the pristine MoS$_2$ and hybrid MoS$_2$/rubrene-patch (with three different thicknesses t_{R1}, t_{R2}, and t_{R3}) TFTs under light irradiation (λ = 455 nm and P_{in} = 15 mW/cm^2). R is an electrical response to the incident light, which is defined as $R \equiv (I_{light} - I_{dark})/P_{in}$. For the pristine MoS$_2$ TFTs, R rapidly increased with negative V_G values and then saturated to ~40 mA/W with the increase in the positive V_G values, as shown in Fig. 5 (open square markers). After attaching the rubrene patches, the R values of the hybrid MoS$_2$/rubrene-patch TFTs increased over the whole V_G range, increasing particularly strongly (reaching a value of 100) in the I_{OFF} regime ($V_G \leqslant$ –15 V). The R values also increased on increasing the rubrene-patch thickness, indicating the efficient generation of photoinduced charge carriers. The saturated R values of the pristine MoS$_2$ and hybrid MoS$_2$/rubrene-patch (with thicknesses t_{R1}, t_{R2}, and t_{R3}) TFTs at V_G = 0 V were 33, 112, 184, and 326 mA/W, respectively (in the accumulation region).
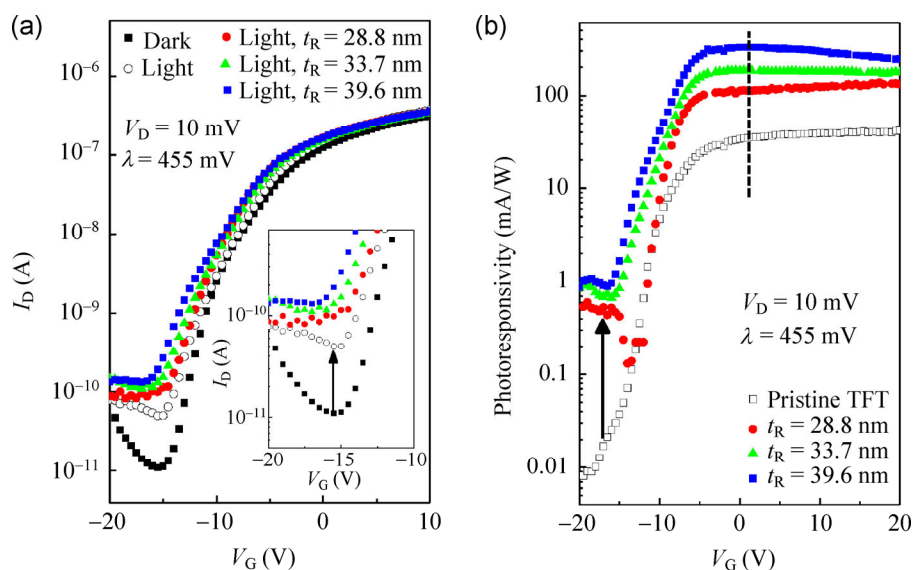

Figure 5 (a) Transfer characteristic curves (I_D versus V_G) in logarithmic scale of the pristine MoS$_2$ and hybrid MoS$_2$/rubrene-patch (three different thicknesses: t_{R1} = 28.8 nm, t_{R2} = 33.7 nm, and t_{R3} = 39.6 nm) TFTs in the dark and under light irradiation (λ = 455 nm). Inset: Magnified I_D–V_G transfer characteristic curves in the OFF regime. (b) Photoresponsivity curves as a function of the gate bias of the pristine MoS$_2$ (open markers) and hybrid MoS$_2$/rubrene-patch (t_{R1}, t_{R2}, and t_{R3}) TFTs under light irradiation (λ = 455 nm). The dashed line represents the boundary of the OFF and ON state regimes.

Therefore, the photoresponsivity of the hybrid TFTs obviously increased with increasing the rubrene-patch thickness and the gate bias because of more productive photoinduced CT from the rubrene patches and lowering of the potential barriers. The photoresponsivity of the pristine and hybrid TFTs as a function of source-drain bias (V_D) is shown in Fig. S4 (in the ESM). The photoresponsivities of the hybrid TFT were higher than those of the pristine one in the whole range of V_D.

The photoresponsivities of our hybrid MoS$_2$/rubrene-patch TFTs showed poorer performance compared with a silicon photodiode ($R \cong 300$ A/W); however, they were better than those in a previous report using multilayer MoS$_2$ TFTs ($R \cong 80$ mA/W). In this study, we have demonstrated that the charge mobility and R values of the MoS$_2$ TFTs were improved by the hybridization of the p-type organic rubrene patches. Our results provide a novel way of tuning the photoresponsive electrical characteristics of MoS$_2$-based devices through hybridization with organic semiconductors. Optimization of the optoelectronic characteristics of the hybrid MoS$_2$ devices will be further studied.

4   Conclusions

We have fabricated new TFTs using 2D hybrid MoS$_2$/rubrene patches and investigated their photoresponsive electrical characteristics. The charge carrier mobility increased from 34.3 to 42.3 cm^2/V·s, and the photo-responsivity increased from 33 to 326 mA/W as the thickness of the rubrene patches on the MoS$_2$ surface increased up to 39.6 nm. The enhanced charge mobility and photoresponsive electrical characteristics were analyzed in terms of the ground and photoinduced CT effects, which were validated by PL quenching measurements and the decrease in the exciton lifetime measured through the LCM PL and TR-PL experiments, respectively.

Acknowledgements

References

[1]   Geim, A. K.; Novoselov, K. S. The rise of graphene. *Nat. Mater.* **2007**, *6*, 183–191.

[2]   Novoselov, K. S.; Geim, A. K.; Morozov, S. V.; Jiang, D.; Zhang, Y.; Dubonos, S. V.; Grigorieva, I. V.; Firsov, A. A. Electric field effect in atomically thin carbon films. *Science* **2004**, *306*, 666–669.

[3]   Novoselov, K. S.; Geim, A. K.; Morozov, S. V.; Jiang, D.; Katsnelson, M. I.; Grigorieva, I. V.; Dubonos, S. V.; Firsov, A. A. Two-dimensional gas of massless Dirac fermions in graphene. *Nature* **2005**, *438*, 197–200.

[4]   Radisavljevic, B.; Radenovic, A.; Brivio, J.; Giacometti, V.; Kis, A. Single-layer MoS$_2$ transistors. *Nat. Nanotechnol.* **2011**, *6*, 147–150.

[5]   Lembke, D.; Kis, A. Breakdown of high-performance monolayer MoS$_2$ transistors. *ACS Nano* **2012**, *6*, 10070–10075.

[6]   Wang, H.; Yu, L.; Lee, Y. H.; Shi, Y.; Hsu, A.; Chin, M. L.; Li, L. J.; Dubey, M.; Kong, J.; Palacios, T. Integrated circuits based on bilayer MoS$_2$ transistors. *Nano Lett.* **2012**, *12*, 4674–4680.

[7]   Brivio, J.; Alexander, D. T. L.; Kis, A. Ripples and layers in ultrathin MoS$_2$ membranes. *Nano Lett.* **2011**, *11*, 5148–5153.

[8]   Li, H.; Yin, Z.; He, Q.; Li, H.; Huang, X.; Lu, G.; Fam, D. W. H.; Tok, A. I. Y.; Zhang, Q.; Zhang, H. Fabrication of single- and multilayer MoS$_2$ film-based field-effect transistors for sensing NO at room temperature. *Small* **2012**, *8*, 63–67.

[9]   Perkins, F. K.; Friedman, A. L.; Cobas, E.; Campbell, P. M.; Jernigan, G. G.; Jonker, B. T. Chemical vapor sensing with monolayer MoS$_2$. *Nano Lett.* **2013**, *13*, 668–673.

[10]   Gourmelon, E.; Lignier, O.; Hadouda, H.; Couturier, G.; Bernède, J. C.; Tedd, J.; Pouzet, J.; Salardenne, J. MS$_2$ (M = W, Mo) photosensitive thin films for solar cells. *Sol. Energy Mater. Sol. Cells* **1997**, *46*, 115–121.

[11]   Buscema, M.; Barkelid, M.; Zwiller, V.; Van Der Zant, H. S. J.; Steele, G. A.; Castellanos-Gomez, A. Large and tunable

photothermoelectric effect in single-layer MoS$_2$. *Nano Lett.* **2013**, *13*, 358–363.

[12] Mak, K. F.; Lee, C.; Hone, J.; Shan, J.; Heinz, T. F. Atomically thin MoS$_2$: A new direct-gap semiconductor. *Phys. Rev. Lett.* **2010**, *105*, 136805.

[13] Ghatak, S.; Pal, A. N.; Ghosh, A. Nature of electronic states in atomically thin MoS$_2$ field-effect transistors. *ACS Nano* **2011**, *5*, 7707–7712.

[14] Kim, S.; Konar, A.; Hwang, W. S.; Lee, J. H.; Lee, J.; Yang, J.; Jung, C.; Kim, H.; Yoo, J. B.; Choi, J. Y. et al. High-mobility and low-power thin-film transistors based on multilayer MoS$_2$ crystals. *Nat. Commun.* **2012**, *3*, 1011.

[15] Sreeprasad, T. S.; Nguyen, P.; Kim, N.; Berry, V. Controlled, defect-guided, metal-nanoparticle incorporation onto MoS$_2$ via chemical and microwave routes: Electrical, thermal, and structural properties. *Nano Lett.* **2013**, *13*, 4434–4441.

[16] Choi, W.; Cho, M. Y.; Konar, A.; Lee, J. H.; Cha, G. B.; Hong, S. C.; Kim, S.; Kim, J.; Jena, D.; Joo, J. et al. High-detectivity multilayer MoS$_2$ phototransistors with spectral response from ultraviolet to infrared. *Adv. Mater.* **2012**, *24*, 5832–5836.

[17] Lopez-Sanchez, O.; Lembke, D.; Kayci, M.; Radenovic, A.; Kis, A. Ultrasensitive photodetectors based on monolayer MoS$_2$. *Nat. Nanotechnol.* **2013**, *8*, 497–501.

[18] Lin, M. W.; Liu, L.; Lan, Q.; Tan, X.; Dhindsa, K. S.; Zeng, P.; Naik, V. M.; Cheng, M. M. C.; Zhou, Z. Mobility enhancement and highly efficient gating of monolayer MoS$_2$ transistors with polymer electrolyte. *J. Phys. D: Appl. Phys.* **2012**, *45*, 345102.

[19] Cho, M. Y.; Kim, S. J.; Han, Y. D.; Park, D. H.; Kim, K. H.; Choi, D. H.; Joo, J. Highly sensitive, photocontrolled, organic thin-film transistors using soluble star-shaped conjugated molecules. *Adv. Funct. Mater.* **2012**, *18*, 2905–2912.

[20] Kang, H. S.; Lee, J. W.; Kim, M. K.; Joo, J.; Ko, J. M.; Lee, J. Y. Electrical characteristics of pentacene-based thin film transistor with conducting poly(3,4-ethylenedioxythiophene) electrodes. *J. Appl. Phys.* **2006**, *100*, 064508.

[21] Cho, E. H.; Kim, B. G.; Jun, S.; Lee, J.; Park, D. H.; Lee, K. S.; Kim, J.; Kim, J.; Joo, J. Remote biosensing with polychromatic optical waveguide using blue light-emitting organic nanowires hybridized with quantum dots. *Adv. Funct. Mater.* **2014**, *24*, 3684–3691.

[22] Peumans, P.; Uchida, S.; Forrest, S. R. Efficient bulk heterojunction photovoltaic cells using small-molecular-weight organic thin films. *Nature* **2003**, *425*, 158–162.

[23] Gommans, H.; Schols, S.; Kadashchuk, A.; Heremans, P.; Meskers, S. C. J. Exciton diffusion length and lifetime in subphthalocyanine films. *J. Phys. Chem. C* **2009**, *113*, 2974–2979.

[24] Mönch, W. Valence-band offsets and Schottky barrier heights of layered semiconductors explained by interface-induced gap states. *Appl. Phys. Lett.*, **1998**, *72*, 1899.

[25] Sillen, A.; Engelborghs, Y. The correct use of "average" fluorescence parameters. *Photochem. Photobiol.* **1998**, *67*, 475–486.

[26] Najafov, H.; Lee, B.; Zhou, Q.; Feldman, L. C.; Podzorov, V. Observation of long-range exciton diffusion in highly ordered organic semiconductors. *Nat. Mater.* **2010**, *9*, 938–943.

[27] Müller, A. M.; Avlasevich, Y. S.; Müllen, K.; Bardeen, C. J. Evidence for exciton fission and fusion in a covalently linked tetracene dimer. *Chem. Phys. Lett.* **2006**, *421*, 518–522.

[28] Kim, J. H.; Yun, S. W.; An, B. K.; Han, Y. D.; Yoon, S. J.; Joo, J.; Park, S. Y. Remarkable mobility increase and threshold voltage reduction in organic field-effect transistors by overlaying discontinuous nano-patches of charge-transfer doping layer on top of semiconducting film. *Adv. Mater.* **2013**, *25*, 719–724.

[29] Walzer, K.; Maennig, B.; Pfeiffer, M.; Leo, K. Highly efficient organic devices based on electrically doped transport layers. *Chem. Rev.* **2007**, *107*, 1233–1271.

[30] Qi, Y.; Sajoto, T.; Kröger, M.; Kandabarow, A. M.; Park, W.; Barlow, S.; Kim, E. G.; Wielunski, L.; Feldman, L. C.; Bartynski, R. A. et al. A molybdenum dithiolene complex as p-dopant for hole-transport materials: A multitechnique experimental and theoretical investigation. *Chem. Mater.* **2009**, *22*, 524–531.

[31] Shi, Y.; Huang, J. K.; Jin, L.; Hsu, Y. T.; Yu, S. F.; Li, L. J.; Yang, H. Y. Selective decoration of Au nanoparticles on monolayer MoS$_2$ single crystals. *Sci. Rep.* **2013**, *3*, 1839.

[32] Liu, H.; Neal, A. T.; Ye, P. D. Channel length scaling of MoS$_2$ MOSFETs. *ACS Nano* **2012**, *6*, 8563–8569.

[33] Perera, M. M.; Lin, M. W.; Chuang, H. J.; Chamlagain, B. P.; Wang, C.; Tan, X.; Cheng, M. M. C.; Tománek, D.; Zhou, Z. Improved carrier mobility in few-layer MoS$_2$ field-effect transistors with ionic-liquid gating. *ACS Nano* **2013**, *7*, 4449–4458.

[34] Late, D. J.; Liu, B.; Matte, H. S. S. R.; Dravid, V. P.; Rao, C. N. R. Hysteresis in single-layer MoS$_2$ field effect transistors. *ACS Nano* **2006**, *6*, 5635–5641.